Flexural behaviour of hybrid steel-GFRP reinforced concrete continuous T-beams

Hanady Almahmood, Ashraf Ashour, Therese Sheehan

Miss Hanady Almahmood
PhD research student, Civil Engineering Department, Faculty of Engineering and Informatics,
University of Bradford, Bradford, West Yorkshire, BD7 1DP,
UK Email address: h.a.a.almahmood@gmail.com

Prof Asharf Ashour
Professor of Structural Engineering, Civil Engineering Department, Faculty of Engineering and Informatics,
University of Bradford, Bradford, West Yorkshire, BD7 1DP,
UK Email address: A.F.Ashour@bradford.ac.uk

Dr Therese Sheehan
Lecturer in Structural Engineering, Civil Engineering Department, Faculty of Engineering and Informatics,
University of Bradford, Bradford, West Yorkshire, BD7 1DP,
UK Email address: Sheehan@bradford.ac.uk

* Corresponding author
Miss Hanady Almahmood
Email: h.a.a.almahmood@gmail.com
Phone: +44 07388307089

Abstract

This paper presents test results of six full scale reinforced concrete continuous T beams. One beam was reinforced with glass fibre reinforced polymer (GFRP) bars while the other five beams were reinforced with a different combination of GFRP and steel bars. The ratio of GFRP to steel reinforcement at both mid-span and middle-support sections was the main parameter investigated. The results showed that adding steel reinforcement to GFRP reinforced concrete T-beams improves the flexural stiffness, ductility and serviceability in terms of crack width and deflection control. However, the moment redistribution at failure was limited because of the early yielding of steel reinforcement at a beam section that does

not reach its moment capacity and could still carry more loads due to the presence of FRP reinforcement.
The experimental results were compared with the ultimate moment prediction of ACI 440.2R-17, and with the existing theoretical equations for deflection prediction. It was found that the ACI 440.2R-17 reasonably estimated the moment capacity of both mid-span and middle support sections. Conversely, the available theoretical deflection models underestimated the deflection of hybrid reinforced concrete T-beams at all load stages.

Keywords: Fibre-reinforced polymer, hybrid reinforced system, continuous beams, T-section, moment redistribution.

1. Introduction

Steel reinforcement corrosion is a major cause of deterioration; consequently, failure of reinforced concrete structures [1]. Therefore, fibre reinforced polymer (FRP) bars have been introduced and accepted as an alternative to steel reinforcement because of their natural corrosion resistance. However, the linear elastic behaviour up to failure and the low elastic modulus of FRP bars under tensile stress are responsible for the brittleness, large deflections and wide cracks associated with FRP-reinforced concrete (RC) structures. Furthermore, since most of concrete structures are continuous elements, the use of FRP reinforcement affects the ability of these structures to redistribute moments between critical sections in comparison with under–reinforced steel structures, leading to unexpected failure without sufficient warning [2, 3]. As a result, several methods have been recommended to improve the ductility of FRP-RC beams [4], including the combined use of FRP and steel reinforcement.

Hybrid FRP/steel reinforcement system was firstly proposed in 1995 [5], where steel reinforcement was placed at an inner level, and FRP bars were located at the outer level, achieving the required strength as well as sufficient corrosion protection to steel reinforcement. Since then, the flexural behaviour of hybrid reinforced concrete beams has been widely investigated, in particular during the past two decades [6-13], focusing mainly on simply supported concrete beams of rectangular sections. The results showed that using steel reinforcement in a

hybrid reinforcement system improves the ductility of FRP-RC beams, and the contribution of FRP reinforcement increases the ultimate load capacity. Furthermore, using this arrangement of reinforcement offers improved serviceability in terms of crack width and deflection control, and a longer service life compared to steel–RC structures. Lately, the flexural performance of hybrid reinforcement system in continuous RC rectangular beams was investigated [14], considering different configurations of FRP and steel reinforcement ratio. It was shown that the reinforcement ratios were the main factor in ensuring adequate ductility of hybrid reinforced continuous concrete beams.

In practice, RC structural systems are almost monolithic; as a result, part of the slab acts together with the underlying beams to form a T- beam section, which represents the reality of structures more than rectangular beams. The behaviour of T-section beams is different from that of rectangular beams due to the effect of the flange part in resisting compression. In continuous beams with a T section, both mid-span and middle-support regions behave as a T section before cracking, while after cracking the mid-span section performs as a T- section and the hogging moment section acts as a rectangular section. Due to these dissimilarities in performance between continuous T and rectangular beams, this study, a first of its kind, aims to investigate the behaviour of hybrid reinforced concrete continuous T-beams. Five continuous concrete T-beams reinforced with different combinations of GFRP/steel reinforcement at critical sections and one beam reinforced with GFRP bars were tested to failure. Test results in terms of crack prorogation, mode of failure, crack width, load-capacity, load-deflection, and moment redistribution are presented and discussed. Additionally, the experimental results were compared with the ultimate moment prediction of the ACI 440.2R-17, and with the available theoretical equations for deflection prediction.

2. Experimental programme

2.1 Test specimens

The experimental programme included six continuous reinforced concrete T beams. The dimensions and reinforcement details of each specimen are presented in Fig. 1. All beams had a T-section, with 200×200 mm for the web part

and 500 ×100 mm for the flange part. The total length of each beam was 5100 mm, including two spans of 2400 mm and two overhangs of 150 mm, as shown in Fig. 1-a. The main investigated parameter in this experimental programme was the flexural reinforcement ratio at both mid-span and middle-support sections. Five beams were reinforced with a different combination of GFRP and steel bars at the critical sections, while one beam was reinforced with pure GFRP bars for comparative purposes. The mid-span cross-section details of the tested beams are presented in Fig. 1-b. For all beams, the top reinforcement was curtailed according to the development length provided by CSA A23.3-4 [15], excluding the two bars which were used as stirrup hangers. However, the bottom reinforcement extended throughout the full beam length, as shown in Figure 1-a.

The reinforcement details for all tested beams are summarized in Table 1. The design of the test specimens is based on the sectional analysis of hybrid reinforced concrete sections [16]. Figs. 2 and 3 show the mode of failure for various combinations of steel and FRP reinforcement ratios for mid-span and middle-support sections, respectively, where the reinforcement ratios are defined Eqs. 1 and 2 for sagging and hogging sections, respectively.

$$\rho_{sagging} = \frac{A_{s,f}}{b_f d} \quad (1)$$

$$\rho_{hogging} = \frac{A_{s,f}}{b_w d} \quad (2)$$

where $\rho_{sagging}$ and $\rho_{hogging}$ are the reinforcement ratios of the sagging and hogging moment sections respectively, $A_{s,f}$ is the area of either steel or FRP reinforcement, b_f and b_w are the flange and web width respectively, d is the depth of FRP reinforcement.

The web width is used for the middle-support section, while the flange width is used for the mid-span section since it is the effective concrete part at the compression side. These design charts were prepared for a target compressive strength of 40 MPa; however, to avoid FRP rupture before concrete crushing, the design charts were also produced for a concrete compressive strength of 60 MPa. The reinforcement properties that were used for the design of these charts are listed in Table 2.

All hybrid-reinforced sections were designed to fail due to steel yielding followed by concrete crushing before FRP rupture. The reinforcement ratio for the control hybrid-reinforced specimen, beam BH1, was chosen based on the limitation shown in Figs. 2 and 3 of the sagging and hogging moment sections. Beam BG was reinforced with pure GFRP reinforcement for comparative purposes; therefore, it was designed to achieve a similar moment capacity to beam BH1 at both critical sections. The beam was designed to fail due to concrete crushing at the mid-span and middle-support sections, as the reinforcement ratio at both sections was larger than the balanced reinforcement ratio estimated by ACI 440-015 [17]. For Beams BH2 and BH3, the reinforcement ratio was kept the same as beam BH1 at the mid-span section. However, beam BH2 was reinforced with higher GFRP reinforcement ratio at the middle-support section, while beam BH3 was reinforced with higher steel reinforcement ratio at the middle-support section. On the contrary, beams BH4 and BH5 were reinforced with the opposite arrangement to BH2 and BH3. The reinforcement ratio of BH4 and BH5 was kept the same as beam BH1 at the middle-support section, while it was changed at the mid-span section. Beam BH4 was reinforced with a higher GFRP reinforcement ratio, whereas beam BH5 was reinforced with a higher steel reinforcement ratio.

Compared with longitudinal reinforcement, steel stirrups would be more exposed to corrosion due to less concrete cover. However, the use of GFRP stirrups whose dimensions should be designed specifically for each project would incur high cost and complicated manufacturing process. GFRP stirrups at the location of the bend become weak, promoting local failure. Alternatively, the performance of straight FRP bars as shear reinforcement cannot be guaranteed due to the anchorage issues [18]. Therefore, steel stirrups of Ø10 mm at a spacing of 75 mm were used as shear reinforcement for all tested beams to prevent shear failure. The slab reinforcement was chosen to represent the lateral and main slab reinforcement in a typical RC floor. The main and lateral slab reinforcement satisfied the CSA-S806-12 [19] design code criteria for minimum slab reinforcement and minimum spacing. The lateral reinforcement was GFRP bars of Ø10 mm spaced at 150 mm at the top and bottom of the flange. Besides, two-

GFRP bars of Ø10mm were chosen as distributed slab reinforcement, as illustrated in Fig. 1-b.

2.2 Materials

The tensile properties of GFRP bars were obtained according to ACI 440.3R-12 [20]. The GFRP bars ends were embedded in strong steel tubes filled with special expansive material to protect the bars from early failure caused by the steel jaws of the testing machine. The tensile test results of steel and GFRP bars are listed in Table 2.

Ready-mix concrete was used to cast the specimens with the maximum coarse aggregate size of 10 mm. The average concrete compressive strength was found by testing three cubes of 100 mm under compressive force, while the average tensile strength was found by testing three concrete cylinders, 150 mm diameter by 300 mm height, at the day of each beam test. The results of concrete properties are presented in Table 3.

2.3 Test setup

The beams test-rig setup is shown in Fig. 4. A strong steel spreader beam was used to spread the loads from the 1000 kN hydraulic jack to the loading plates, as shown in Fig. 4. The centre of the loading plates was set in the middle of each span by using special plaster material to avoid any movement of the plates during the test and to spread the applied load evenly. The beams were supported using roller supports at the ends and a hinge support at the middle. The top plates were 150 mm width by 600 mm length to cover the full flange width, while the bottom end-plates were 200 mm wide by 200 mm long to include the entire web width. All steel plates had a 40 mm thickness to avoid any plate deformation during the test.

Two load cells were used at the end supports to measure the end reactions of the beams and to allow calculation of the internal forces. Additionally, three digital cameras were used to monitor the crack width during the test; two of them were placed at the mid-span sections, and one was placed at the front of the middle-support section. Furthermore, four linear variable differential transducers (LVDTs) were used to track the deflection of the beams during tests. Two of them

were placed at the critical sections at the mid-span, while the top LVDTs set at the end support to check the stability of the system, as shown in Fig. 4. Strain gauges were attached to the reinforcement critical positions at the mid-span and middle-support sections to measure the strain values in reinforcing bars during the test. Throughout the tests, the cracks were manually marked on the face of the beam, while the full system of LVDTs, strain gauges, load cells and the hydraulic jack were connected to the data logger to record the readings at every load increment.

3. Experimental results

3.1 Crack propagation and modes of failure

The crack propagation for the tested beams was recorded and sketched manually during the loading process, as shown in Fig. 5. The first visible cracks at both sagging and hogging moment sections are listed in Table 4. The contra-flexure points in accordance to the elastic moment distribution for a two-span beam having a constant flexural stiffness were also identified in Fig. 5. These points clearly signify the switch from bottom to top flexural cracking, agreeing with the crack pattern observed in experiments. All beams started to develop vertical flexural cracks at the critical sections of the tensile zone, which later extended to the compression zone of each section. As the applied load was increased, the number of cracks increased while the existing cracks developed wider, followed by steel yielding at either the middle-support or the mid-span sections as recorded by the strain gauges for the hybrid reinforced concrete beams. Close to failure, the width of the existing cracks continued to increase until concrete crushing occurred at the middle-support section. In beams BG and BH1, a diagonal shear crack was developed at the middle-support section due to the high shear forces combined with a high moment value at this location. Moreover, the intensity of cracks at the critical sections for beams BH2, BH3, BH4 and BH5 was higher than that of beam BH1 due to the total increase in the load capacity of those beams compared with that of beam BH1.

The first cracks were very thin cracks recorded at the mid-span section of the beams, followed by a vertical flexural crack appeared at the middle-support section for all tested beams. The location of the first cracks at the sagging -

moment section is explained as follows: in contrast to rectangular sections, T-section beams have a lower cracking moment, $\mathrm{M_{cr}}$, for the mid-span section than that of the middle-support section, as calculated in Eq.3. This because the distance from the centroidal axis of the gross section to tension face, y, is higher for the mid-span section than for the middle-support section. As a result, the flexural cracks initiate in the mid-span section before the middle-support section. However, the sagging moment section had many narrow cracks compared to the small number of wider cracks at the hogging moment section for all tested beams. This could be explained because the mid-span section behaves as a T-section after cracking while the section over the middle-support performs as a rectangular section, making the mid-span region stiffer than the middle-support region which caused wider cracks at the middle-support section for all tested beams.

$$\mathrm{M_{cr}} = \frac{0.62\sqrt{f_c`}\,\mathrm{I_g}}{y} \tag{3}$$

where $f_c`$ is the concrete compressive strength, $\mathrm{I_g}$ is the gross moment of inertia and y is the distance from the centroid axis of the gross section to tension face, neglecting reinforcement.

The first cracking moment for beams BH1 and BH4 at the mid-span section is lower than that of other beams. This because both beams had lower compressive strengths than other beams which reduced the cracking moment, as calculated in Eq. 3. However, the readings for the first cracks were taken manually according to the first visual cracks, which was not accurate all the time.

Figs. 6 and 7 show the mode of failure and the deformed shapes for all tested beams, respectively. Beam BG failed by flexural-shear failure, initiating with concrete crushing combined with diagonal shear cracks and FRP rupture at the middle-support section, as shown in Figure 6-a. The crushing of concrete was firstly observed in the middle-support section. However, a diagonal wide shear crack appeared and continued towards the support, leading to rupture of GFRP bars as shown in Fig. 6-a. The mode of failure for beam BH1 was similar to that observed for beam BG, the flexural-tensile cracks initiated at both the mid-span and middle-support sections of beam BH1 and then continued to the compression

side of each section. As the load increased, concrete crushing after steel yielding was observed at the middle support section. At the ultimate failure load, concrete spalling was detected at the middle-support section, which merged directly with a wide diagonal shear crack, as can be seen in Fig. 6-b.

Beams BH2, BH3, BH4 and BH5 demonstrated flexural failure at the middle-support section, as shown in Fig. 6-c, Fig. 6-d, Fig. 6-e, and Fig. 6-f, respectively. The failure started with flexural cracks at the tensile zone of the critical sections, which later continued to the compression side of each section, followed by steel yielding at the middle-support and mid-span sections as recorded by the strain gauges. Finally, concrete crushing was observed at the middle-support section at the ultimate failure load.

3.2 Cracks width and reinforcement strain

Figs. 8 and 9 show the average measured crack width for all tested beams against the total load at both the middle-support and mid-span sections, respectively. Generally, the cracks at the middle-support section were wider than those at the mid-span section due to the high reinforcement ratio at the sagging moment section that controls the crack width at this region until failure. Additionally, beam BG exhibited the widest crack width at the middle-support and mid-span sections compared with hybrid-reinforced beams. The crack width in beam BG was higher than the crack width of beam BH1 at 600 kN at both middle-support and mid-span by 34% and 63%, respectively. This result was expected because of the low axial stiffness of the GFRP bars in beam BG, while the higher stiffness of the added steel bars to beam BH1 reduced the crack width significantly. This result confirms the efficiency of using hybrid steel/GFRP reinforcement in significantly reducing the crack width

Increasing either GFRP or steel reinforcement ratio in the middle-support section had a limited effect in reducing the crack width than adding the reinforcement in the mid-span section. There was limited improvement in the crack width of beam BH2, which had 1.33 of that the GFRP reinforcement in BH1 at middle-support section, as can be seen in Fig. 8. Additionally, even though BH3 was reinforced with 2.5 times the steel reinforcement ratio at the middle-support section of BH1, it had only 7% reduction in the crack width at 600 kN than BH1 in middle-support

section, as shown in Fig. 8. This could be explained due to shortening the reinforcement bars at the middle-support section, while in mid-span section the reinforcement bars have been extended along the beam. Additionally, increasing steel reinforcement is more effective in reducing the crack width than increasing the GFRP reinforcement ratio, as seen for beams BH3 and BH5 in Figs. 8 and 9, respectively.

Overall, the width of cracks in the hogging-moment section was higher than the width of the crack in the sagging-moment section, because the mid-span section behaves as a T-section after cracking while the section over the middle-support acts as a rectangular section, making the mid-span region stiffer than middle-support region, which results in wider cracks at the middle-support section for all tested beams. The crack width ranged between 0.1 mm to 4 mm in the hogging-moment section, while it was within the limit of 0.09 mm to 3.3 mm in the sagging-moment section.

Figs. 10 and 11 show the recorded strain values against the total applied load for top and bottom of steel bars, respectively. The strain values were insignificant before cracking, whereas a rapid increase in the reinforcement strain was observed at both regions after the cracks formed, followed by steel yielding at the early stage of the total load. For beams BH1 and BH2, the strain readings for steel bars were presented at one location only because the strain gauges at other locations were damaged during the casting or testing processes. All hybrid-reinforced beams exhibited early steel yielding before reaching the ultimate load capacity, as listed in Table 4. In beams BH4 and BH5, steel yielded at the hogging-moment section before the sagging-moment section because of the variation of the steel reinforcement ratio between the two sections. On the contrary, beam BH3 experienced steel yielding at the sagging-moment section earlier than hogging moment section, due to the high steel reinforcement ratio at the middle-support section, which in turn delayed the steel yielding at this region.

Figs. 12 and 13 show the recorded strain values against the total applied load for top and bottom of GFRP bars, respectively. The GFRP reinforcement strain was almost similar for all tested specimens at the mid-span section except for beam BH4, as shown in Fig. 12. This because of using the same longitudinal GFRP reinforcement ratio for all beams except for beam BH4, which had the highest

GFRP reinforcement ratio in the mid-span section. However, the strain readings for GFRP bars in beam BH4 were not presented at the middle-support section because the strain gauges at this location were damaged during the casting or testing processes. Furthermore, it can be seen increasing the longitudinal GFRP reinforcement ratio at the middle-support section had a limited effect on reducing the tensile reinforcement strain, as seen for beam BH2 in Fig.13. This could be explained as a result of shortening the reinforcement bars at the middle-support section, while in mid-span section the reinforcement bars have been extended along the beam.

3.3 Load capacity

The total load capacities of the tested beams are presented in Table 4. Although beams BH1 and BG were designed to achieve the same moment capacity at the critical section, the total load capacity of beam BH1 was higher than that of beam BG by 10.8%, indicating that the ductility of GFRP-RC beams was enhanced by adding steel reinforcement. The effect of increasing either GFRP or steel reinforcement ratio at the middle-support section led to increase the ultimate load capacity of the tested beams. The enhancement in the load capacity was 11% for beam BH2 where the GFRP reinforcement ratio was 1.33 of that in beam BH1. In addition, the improvement was 17.5 % for BH3, which was reinforced with 2.5 of the steel reinforcement ratio in beam BH1. Similarly, increasing either the GFRP or steel reinforcement ratio at mid-span section improved the ultimate load capacity of hybrid-reinforced beams. The enhancement in the total load capacity was 21.4% and 20.4 % for beams BH4 and BH5 that were reinforced with 1.33 of the GFRP and steel reinforcement ratio of that in beam BH1, respectively.

The previous results indicate that increasing the amount of either GFRP or steel at the mid-span section is more effective in enhancing the load capacity of the beams than that at the middle-support section. This may be attributed to the structural system of the tested two-span beam; in such case the mid-span section moment has a more contribution than that of the middle-support moment to the total applied load, P_{Up}, as calculated in Eq. 4.

$$P_{Up} = \frac{2}{l}\left(M_{hogging} + 2M_{sagging}\right) \quad (4)$$

where $M_{hogging}$ and $2M_{sagging}$ are the moment capacity for the hogging and sagging moments sections, respectively.

3.4 Load-deflection response

A graph showing the total applied load against the defection at the mid-span section of the tested beams is presented in Fig. 14. The deflection at the middle section of each span was continuously monitored using LVDTs as shown in Fig. 14-a for beams BH1 and BH2, indicating close similarity of deflection measurements at each mid span section. Therefore, only one span deflection measurements are presented in Fig. 14-b for all beams tested. No movement was detected by the LVDTs at the beam end supports, confirming no relative settlement at supports. The load-deflection response of the tested beams is divided into three categories, namely the initial linear trend before cracking, non-linear response after cracking, and softening after the ultimate load. Both hybrid- and GFRP reinforced concrete beams tested exhibited stiffness reduction after cracking. However, hybrid reinforced concrete beams showed a further stiffness reduction, initiated after the steel yielding point and continued to the ultimate load.

The stiffness of the tested beams was varied based on the reinforcement ratio. The control hybrid reinforced beam, beam BH1, showed higher stiffness than beam BG that was reinforced with pure GFRP bars, due to the elastic modulus of steel reinforcement that is approximately five times higher than that of GFRP bars. Furthermore, all hybrid reinforced beams had similar flexural rigidity up to a certain point. After that, the effect of increasing either the GFRP or steel reinforcement ratio at the middle-support or mid-span section improved the flexural stiffness of the tested beams. The flexural stiffness of beams BH2, BH3, BH4 and BH5 was improved compared with beam BH1; therefore, the mid-span deflection was reduced at the same value of the load.

The serviceability requirement for the deflection at the service load (0.67 of ultimate load) according to CSA S806-12[19] varied between 5 mm (span/480) and 13.3 mm (span/180), taking into consideration the structural member function. The deflections of beams BH1, BH2, BH3, B4, B5 at the service load were 5.5 mm, 5.64 mm, 6.3 mm, 6.1 mm and 5.6 mm, respectively, showing slight

un-satisfaction of deflection at serviceability condition. However, the deflection can be reduced by changing the reinforcement ratio of the designed beams.

3.5 Moment redistribution and load–reaction

Fig. 15 shows the total applied loads against the experimental and elastic end-supports reactions for all tested beams. The experimental reaction is calculated using the load cell readings at the ends of the beams, while the elastic reaction is found by elastic theory, which is equal to:

$$R = \frac{5}{16} PL \tag{5}$$

where R is the elastic reaction, P is the span load and L is the span length.

The moment redistribution of tested beams is presented in Fig. 16 using Eq. 6. A positive moment redistribution value means that the region has redistributed moment while a negative value means the region has gained moment.

$$M.R = \frac{M_e - M_{ex}}{M_e} 100\% \tag{6}$$

where $\mathrm{M.R}$ is the moment redistribution value, M_e is the elastic moment found by elastic theory which is equal to $0.156\mathrm{PL}$ and $0.188\mathrm{PL}$ for the sagging and the hogging moment sections respectively, and M_{ex} is the experimental moment that is found by using the experimental reaction values.

From Fig. 15, it can be seen that the experimental reaction of beam BG followed the elastic reaction until failure with no sign of moment redistribution. The same result can be seen in Fig. 16, where the elastic and experimental moments remained almost the same for this beam. Beam BH1, which was designed to have the same moment capacity as beam BG at both critical sections, showed a small moment redistribution of 5.47 % from the hogging-moment section to the sagging-moment section. This enhancement is due to adding steel reinforcement, improving the ductility of the beam compared to beam BG. The low value of moment redistribution in beam BH1 could be explained due to the early yielding of steel reinforcement while the section did not reach its full capacity due to the reserve strength of FRP reinforcement in tension and concrete in compression. Therefore, no moment redistribution at failure took place due to yielding of steel reinforcement as steel yielding occurred at early stage. However,

stiffness reduction due to steel yielding was demonstrated as shown in Fig. 14. This behaviour is different from what expected in under-reinforced steel concrete statically indeterminate beams when steel reinforcement yields at one section that consequently reaches its moment capacity. However, as this section exhibits ductility to allow further increase of loading be carried by other parts of the beam until enough sections reach their capacities to cause failure.

Increasing either GFRP or steel reinforcement ratio in the middle-support section slightly reduces the moment redistribution from the hogging moment section to the sagging moment section, as can be seen for beams BH2 and BH3. The reduction in the moment redistribution value was due to the increase of GFRP or steel reinforcement, which in turn reduced the rotational capacity, and consequently the ductility of this section. For beams BH4 and BH5, the experimental reaction exhibited the largest difference from the elastic reaction after a specific limit, as shown in Fig. 15. The moment redistribution values were 10.3 % and 12.7% from hogging-moment to sagging-moment sections for beams BH4 and BH5, respectively. This result could be explained due to the excessive cracks at the middle-support section for both beams, reducing the flexural stiffness of the beam over this section, and, subsequently, increasing the rotational capacity of the section. Besides, this enhancement could be due to the increase of reinforcement ratio at the mid-span section for both beams, which enhanced the flexural stiffness in this section, and, hence, improved the moment redistribution since it depends mainly on the variation of flexural stiffness between sections [21].

4. Predicted moment capacity

In this section, the moment capacity of the tested beams is calculated using ACI 440.2R-17 [22] for externally bonded FRP concrete beams as it is almost similar to hybrid reinforced concrete beams. The calculation technique used to find the ultimate moment capacity of the section should satisfy strain compatibility and force equilibrium equations. To find the moment capacity, an iterative procedure started with selecting the neutral axis depth of section, followed by finding the strain, stress and forces for each material. For an assumed neutral axis depth, if

the equilibrium of forces is not satisfied, the neutral axis depth should be adjusted and the procedure repeated [16]. Bilinear elastic-perfectly plastic and linear-elastic models were chosen for steel and FRP reinforcement, respectively. While a non-linear stress-strain relationship used for concrete under compression and tension, as shown in Fig. 17. The calculation of the moment capacity of T-section beams depends mainly on the location of the neutral axis depth. The neutral axis depth is located in the flange for the mid-span section, while it is found within the web depth for middle-support section.

Table 5 presents the predicted against the experimental moment capacities for both mid-span and middle-support sections. The average value and the standard deviation of the predicted moment capacities to the experimental moment for the mid-span section of the tested beams are 1.18 and 22.8%, respectively. The predicted moment capacity for the mid-span section is higher than the experimental moment for all tested beams as this section did not reach the full moment capacity at failure. However, the variation between the calculated and experimental moments is higher for beam BG and beam BH1 compared to other specimens, due to the early failure caused by the diagonal shear cracks of both beams at middle-support section.

Although the same stress-strain relationships are used to predict the moment capacity at both mid-span and middle-support sections, the calculated value of moment capacity at the middle-support section is significantly less than the experimental moment for all tested beams. The average and the standard deviation of the calculated moment to the experimental moment capacities are 0.69 and 34.9%, respectively. The improvement in the experimental moment capacity is due to the confinement of concrete provided by the transverse reinforcement and the supporting steel plate at this location, increasing the concrete crushing strain and, hence, the flexural capacity of the hogging moment section. Therefore, the moment capacity of the middle-support section is calculated by using the confined stress-strain relationship for concrete shown in Fig. 17-a. The enhancement in the predicted results by using confined concrete properties is obvious compared to the unconfined properties. The average and the standard deviation of the calculated moment capacity to the experimental moment capacity are 1.03 and 11 %, respectively.

5. Prediction load-deflection response

The short-term deflection of two spans continuous beams with two point loads is calculated using Eq. 7, below:

$$\Delta = \frac{7PL^3}{768E_cI_e} \tag{7}$$

where Δ is the deflection at the middle of span, P is the span load; L is the span length; E_c is the modulus of elasticity of concrete which is equal to $4700\sqrt{f_c`}$; $f_c`$ is the concrete compressive strength in MPa; I_e is the effective moment of inertia of the concrete cross-section. For hybrid reinforced beams, the effective moment of inertia is equal to the gross moment of inertia, $\mathrm{I_g}$, before cracking. However, after cracking, it can be expressed by Bischoff model for deflection prediction [23], Eq. (8) below:

$$I_e = \frac{I_{cr}}{1-\left(1-\frac{I_{cr}}{I_g}\right)\left(\frac{M_{cr}}{M_a}\right)^2} \leq I_g \tag{8}$$

where $\mathrm{I_{cr}}$ is the cracked moment of inertia, which is found based on the elastic analysis of the cracked section transformed into concrete; $\mathrm{I_g}$ is the gross moment of inertia of the section neglecting reinforcement; $\mathrm{M_a}$ is the applied moment on the section; $\mathrm{M_{cr}}$ is the cracked moment of the section.

To include the effect of steel yielding on the deflection prediction of hybrid reinforced beams, Yoon et al. 2011 [11] suggested a new model for the effective moment of inertia based on the Bischoff model, as given by Eq.9.

$$I_e = \frac{I_{cr}}{\frac{I_{cr}}{I_y}+\frac{M_y}{M_a}\left(1-\frac{I_{cr}}{I_y}\right)-\frac{{M_y}^2}{M_a}\left(1-\frac{I_{cr}}{I_y}\right)} \leq I_g \qquad M_a \geq M_y \tag{9}$$

where $\mathrm{M_y}$ is the yielding moment of the section, $\mathrm{I_y}$ is the moment of inertia after steel yielding.

To apply Eq. 8 and Eq. 9 for doubly reinforced concrete T-sections beams; the neutral axis depth, the cracked moment of inertia, and the yielding moment of inertia at both mid-span and middle support sections are summarized in Table 6.

Also, as recommended by CSA A23.3-14 [24] for continuous prismatic members, the effective moment of inertia may be taken as the weighted average of the values for the critical positive and negative moment sections as calculated in Eq. 10.

$$I_e = 0.85I_{em} + 0.15I_{ec} \quad (10)$$

where I_{em} is the value of I_e at mid-span section; I_{ec} is the value of I_e at continuous end (middle-support section).

Fig. 18 shows a comparison between the experimental and predicted load-deflection curves. As shown in the figure, using the gross moment of inertia to predict the deflection before cracking gives a reasonable prediction for the load-deflection response for either GFRP or hybrid-reinforced concrete T beams. After cracking and before steel yielding, the effective moment of inertia changed from I_g to I_e, which explained the first change in the slope of the predicted load-deflection curve. At low load level, the predicted results were in good agreement with the experimental results for all beams. Conversely, as the load increased, it is noticeable that using Bischoff's equation, Eq. 8, underestimated the predicted deflection for all specimens. After steel yielding, Yoon's equation (Eq. 9) is used to predict the deflection of hybrid-reinforced beams, clarifying the sudden change in the slope of the predicted load-deflection after steel yielding. It is clear that using Yoon's equation improved the predicted deflections for hybrid-reinforced beams after steel yielding. The enhancement of the load-deflection response can be clearly seen in beam BH5, which was reinforced with the highest steel reinforcement ratio at the mid-span section. However, the improvement of the load-deflection response of beam BH4 after steel yielding was not as clear as beam BH5. This is because beam BH4 was reinforced with the highest GFRP ratio at the mid-span section, implying that Yoon's equation mainly depends on the steel reinforcement ratio.

6. Ductility

In this section the ductility of the tested specimens was calculated using the energy-based method [25]. The energy ductility index, μ_c, based on the

relationship between the total energy to the elastic energy, as shown in Fig. 19 and calculated by Eq. 11.

$$\mu_c = \frac{1}{2}\left(\frac{E_{total}}{E_{elastic}} + 1\right) \quad (11)$$

where E_{total} is the total energy absorbed by the member, which is equivalent to the area under the load-deflection curve until the failure point and $E_{elastic}$ is the elastic energy released at failure and its part of the total energy calculated by the area of the triangular formed at failure load by a line having the weighted average slop of the two initial straight lines of the load-deflection curves.

The energy concept was applied to the load-deflection curves of the tested beams, as shown in Fig. 20 and the ductility index calculations for the tested specimens is presented in Table 7. The energy index for beam BG was the lowest among the tested specimens, implying least ductility, as listed in Table 7. The enhancement in the ductility index for different beams with respect to that of beam BG is also presented in Table 7. Beams BH1 and BH2 show a slightly higher energy ductility indices of 18.6 % and 19.1%, respectively compared with that of beam BG. Additionally, the higher energy index values for beams BH4 and BH5 are due to the higher values of moment redistribution exhibited by these beams compared to the other specimens, showing that adding steel reinforcement to GFRP-RC beams improves their ductility.

7. Conclusions

Six large-scale continuous reinforced concrete T-beams were tested and analysed. Five beams were reinforced with hybrid steel/GFRP bars while one beam was reinforced with GFRP bars. The main parameter investigated was the ratio of the steel to GFRP reinforcement at both the middle-support and mid-span sections. The following conclusions can be drawn based on the achieved results:

1. Adding steel reinforcement to GFRP-RC T beams improves the ductility and deformability of the beams by preventing the brittle failure of GFRP-RC beams.

2. Adding steel reinforcement to GFRP-RC T beams significantly reduces the crack width. Also, increasing the steel reinforcement is more effective in reducing the crack width than increasing the GFRP reinforcement ratio.

3. Adding steel reinforcement to GFRP-RC T beams enhances the flexural stiffness of the GFRP-RC beams. The HRCT-beams demonstrate smaller deflection compared to GFRP-beams at the same value of the load, due to the elastic modulus of steel reinforcement that is approximately five times higher than that of GFRP bars.

4. Increasing the amount of either GFRP or steel at the mid-span section is more effective in enhancing the load capacity of the beams than that at the middle support section. This may be attributed to the structural system of the tested two-span beam as the mid-span section moment has a greater contribution than that of the middle-support moment to the total applied load.

5. Adding steel reinforcement to continuous GFRP-RCT beams did not achieve considerable moment redistribution due to the early yielding of steel reinforcement while the section did not reach its full capacity due to the reserve strength of FRP reinforcement in tension and concrete in compression.

6. Adding reinforcement to the region from which the moment redistributes reduces the amount of the moment redistribution, because of decreasing the rotational capacity of this section. However, adding reinforcement to the region into which the moment redistributes, improves the achieved amount of moment redistribution.

7. ACI 440.2R-17 reasonably estimated the moment capacity of both mid-span and middle-support sections. However, the accuracy of the results mainly depends on the stress-strain relationship of concrete under compression.

8. Using both Bischoff and Yoon models for cracked moment of inertia calculations underestimated the deflection at all load stages for both GFRP and hybrid reinforced concrete T beams.

Data Availability: The raw/processed data required to reproduce these findings cannot be shared at this time as the data also forms part of an ongoing study.

Reference

1. Böhni, H., *Corrosion in Reinforced Concrete Structures*. 2005: Elsevier Science. ISBN 9781845690434.
2. Habeeb, M. and A.F. Ashour, *Flexural behavior of continuous GFRP reinforced concrete beams.* Journal of Composites for Construction, 2008. **12**(2): p. 115-124.
3. Mahroug, M.E.M., A.F. Ashour, and D. Lam, *Tests of continuous concrete slabs reinforced with carbon fibre reinforced polymer bars.* Composites Part B: Engineering, 2014. **66**: p. 348-357.
4. Wang, H. and A. Belarbi, *Ductility characteristics of fiber-reinforced-concrete beams reinforced with FRP rebars.* Construction and Building Materials, 2011. **25**(5): p. 2391-2401.
5. Arya, C., F. Ofori-Darko, and G. Pirathapan. *27 FRP REBARS AND THE ELIMINATION OF REINFORCEMENT CORROSION IN CONCRETE STRUCTURES*. in *Non-Metallic (FRP) Reinforcement for Concrete Structures: Proceedings of the Second International RILEM Symposium*. 1995. CRC Press.
6. Tan, K. *Behaviour of hybrid FRP-steel reinforced concrete beams*. in *Proc., 3rd Int. Symposium, FRPRCS*. 1997.
7. Arya, C., et al., *TR 55: Design guidance for stengthening concrete structures using fibre composite materials: a review.* Engineering Structures, 2002. **24**(7): p. 889-900.
8. Si-Larbi, A., E. Ferrier, and P. Hamelin, *Flexural behaviour of MRBC beams (multi-reinforcing bars concrete beams), promoting the use of FRHPC.* Composite structures, 2006. **74**(2): p. 163-174.
9. Qu, W., X. Zhang, and H. Huang, *Flexural behavior of concrete beams reinforced with hybrid (GFRP and steel) bars.* Journal of Composites for construction, 2009. **13**(5): p. 350-359.
10. Lau, D. and H.J. Pam, *Experimental study of hybrid FRP reinforced concrete beams.* Engineering Structures, 2010. **32**(12): p. 3857-3865.
11. Yoon, Y.S., et al. *Flexural strength and deflection characteristics of high-strength concrete beams with hybrid FRP and steel bar reinforcement*. in *10th International Symposium on Fiber-Reinforced Polymer Reinforcement for Concrete Structures 2011, FRPRCS-10, in conjunction with the ACI Spring 2011 Convention*. 2011.
12. Yinghao, L. and Y. Yong, *Arrangement of hybrid rebars on flexural behavior of HSC beams.* Composites Part B: Engineering, 2013. **45**(1): p. 22-31.
13. Pang, L., et al., *Design Propositions for Hybrid FRP-Steel Reinforced Concrete Beams.* Journal of Composites for Construction, 2015. **20**(4): p. 04015086.
14. Araba, A.M. and A.F. Ashour, *Flexural performance of hybrid GFRP-Steel reinforced concrete continuous beams.* Composites Part B: Engineering, 2018. **154**: p. 321-336.

15. CSA, *A23. 3-04.* Canadian Standard Association, 2004. **232**.
16. Kara, I.F., A.F. Ashour, and M.A. Köroğlu, *Flexural behavior of hybrid FRP/steel reinforced concrete beams.* Composite Structures, 2015. **129**: p. 111-121.
17. 440.1R-015, A. *Guide for the Design and Construction of structural concrete reinforced with Fiber Reinforced Polymer (FRP) bars (ACI 440.1 R-15)*. American Concrete Institute Farmington Hills, MI.
18. Valivonis, J., et al., *Study on shear resistance of fiberreinforced polymer–reinforced concrete beams.* Advances in Mechanical Engineering, 2015. **7**(7): p. 1687814015593873.
19. CSA-s806, C.S.A., *Design and Construction of Building Structures with Fibre-Reinforced Polymers,(CAN/CSA S806-12).* Canadian Standards Association Mississauga, Ont, 2012.
20. Commitee, A., *440.* Guide Test Methods for Fiber-Reinforced Polymers (FRPs) for Reinforcing or Strengthening Concrete Structures (ACI 440.3 R-12), American Concrete Institute, Detroit, 2012.
21. Oehlers, D., et al., *Moment redistribution in continuous plated RC flexural members. Part 2: Flexural rigidity approach.* Engineering structures, 2004. **26**(14): p. 2209-2218.
22. Committee, A., *Guide for the design and construction of externally bonded FRP systems for strengthening concrete structures (ACI 440.2 R-17).* American Concrete Institute, Farmington Hills, MI, 2017.
23. Bischoff, P.H., *Deflection calculation of FRP reinforced concrete beams based on modifications to the existing Branson equation.* Journal of Composites for Construction, 2007. **11**(1): p. 4-14.
24. Association, C.S., *CSA A23. 3-14: Design of Concrete Structures.* Canadian Standards Association: Toronto, ON, Canada, 2014.
25. Naaman, A. and S. Jeong. *45 STRUCTURAL DUCTILITY OF CONCRETE BEAMS PRESTRESSED WITH FRP TENDONS*. in *Non-Metallic (FRP) Reinforcement for Concrete Structures: Proceedings of the Second International RILEM Symposium*. 1995. CRC Press.
26. Reddiar, M.K.M., *Stress-strain model of unconfined and confined concrete and stress-block parameters.* Diss. Texas A&M University, 2009.
27. Gu, X., X. Jin, and Y. Zhou, *Basic principles of concrete structures*. 2016: Springer. ISBN 3662485656.

Acknowledgments

The corresponding author would like to express his special thanks and gratitude to Applied Science Private University in Jordan for their financial support.

Figures

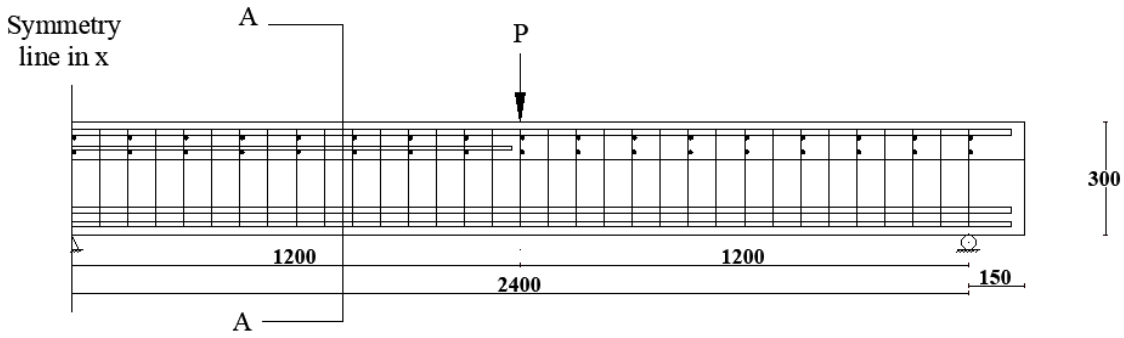

a. Longitudinal reinforcement details section (B-B).

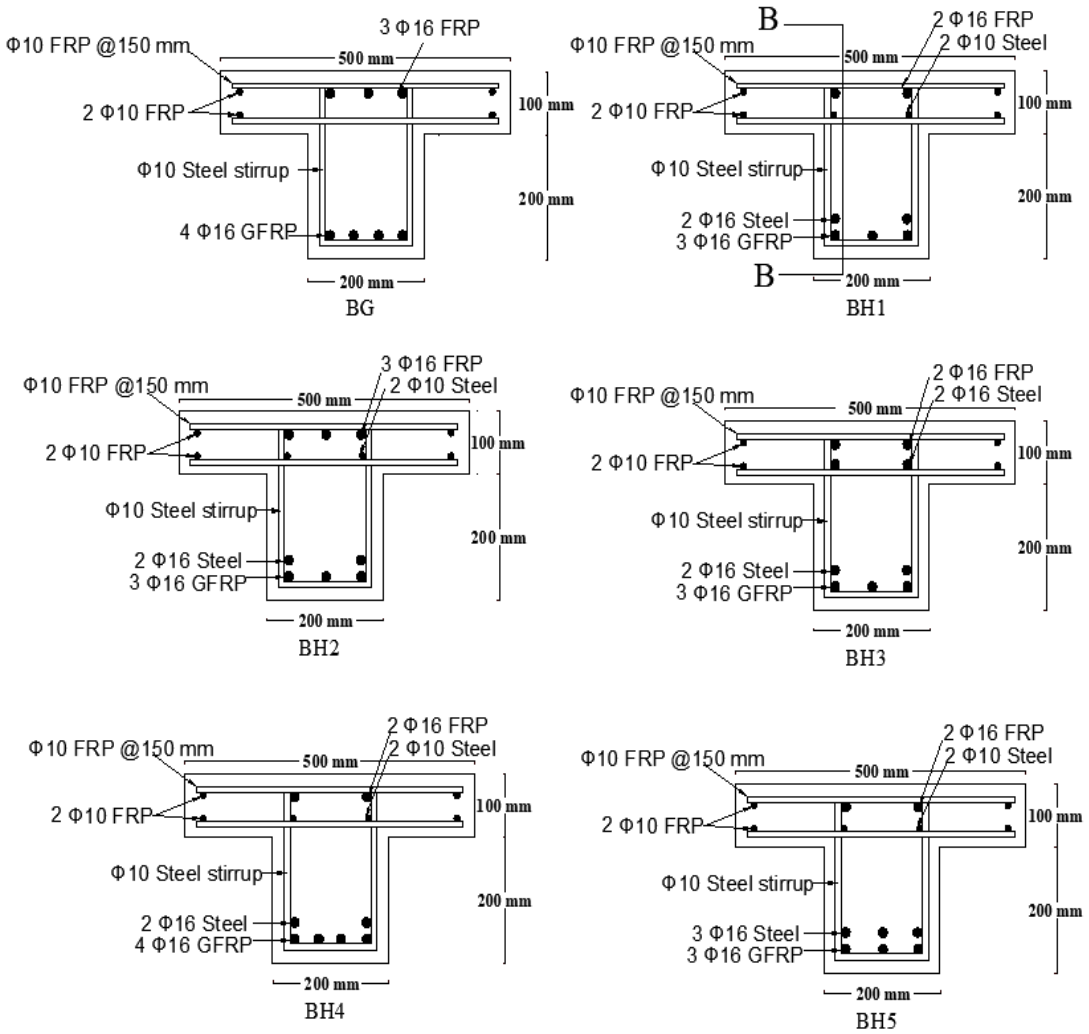

b. Cross-section reinforcement details (section A-A).

Figure 1: Description of the tested specimens (all dimensions in mm).

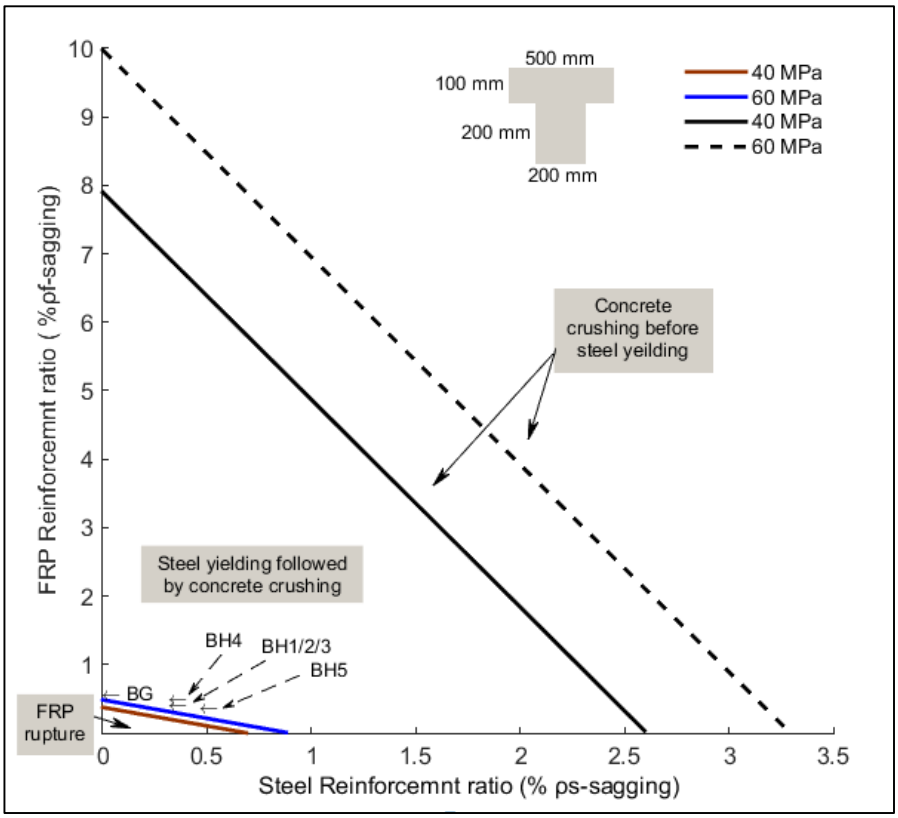

Figure 2: Limitations for modes of failure based on the reinforcement ratio of steel vs GFRP bars (mid-span section).

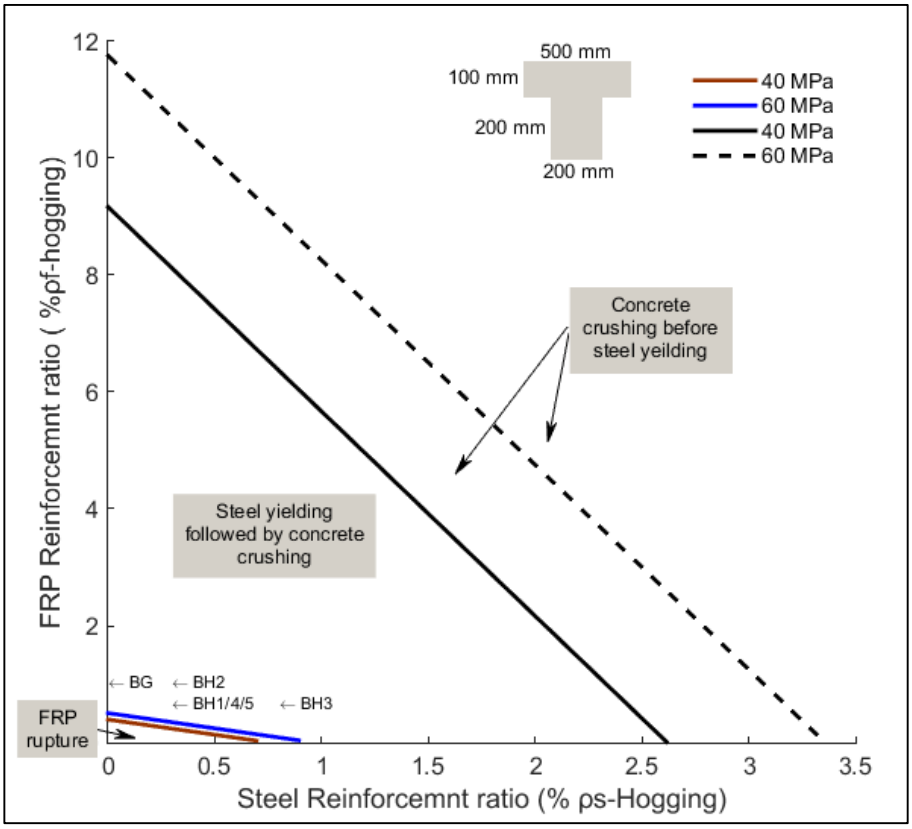

Figure 3: Limitations for modes of failure based on the reinforcement ratio of steel vs GFRP bars (middle-support section).

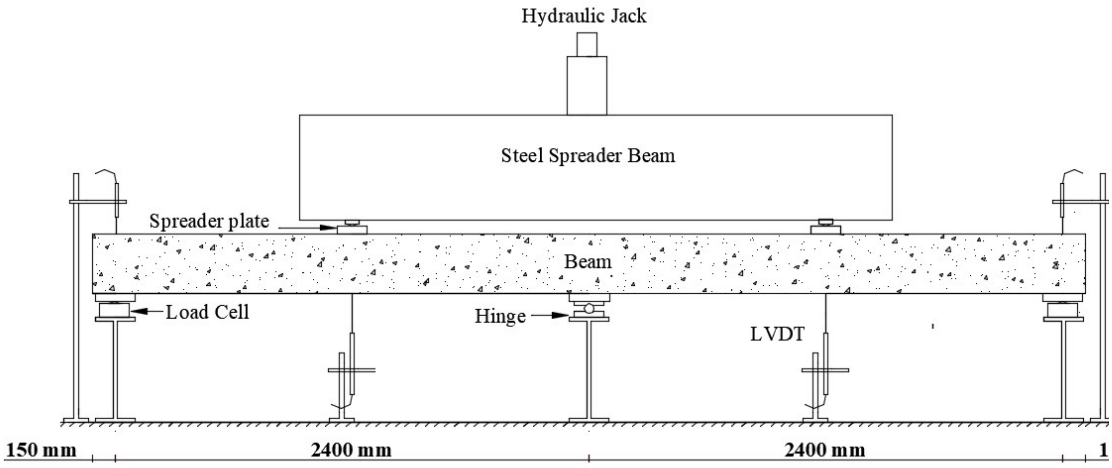

Figure 4: Experimental beam test setup.

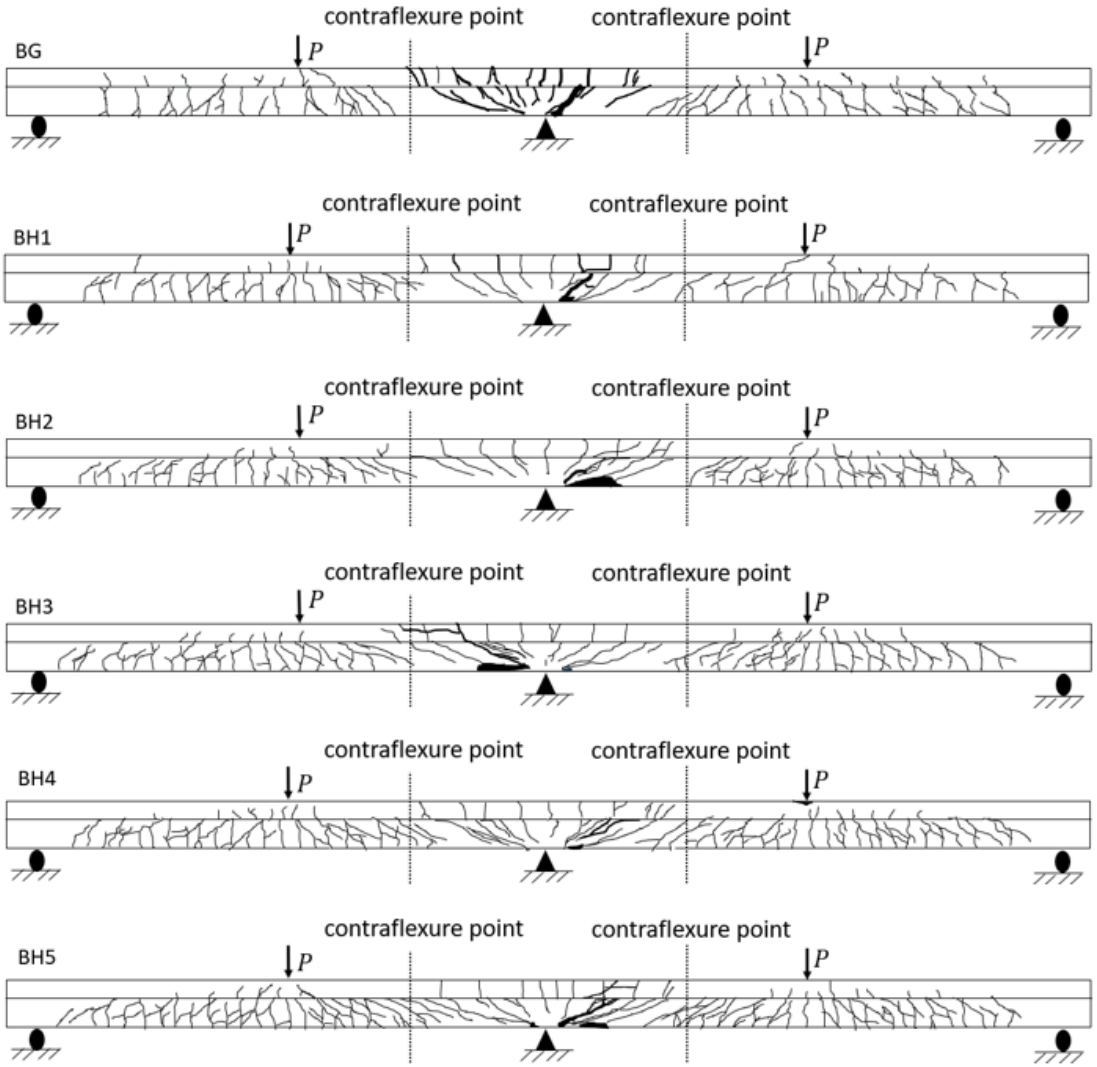

Figure 5: Crack patterns for the tested beams.

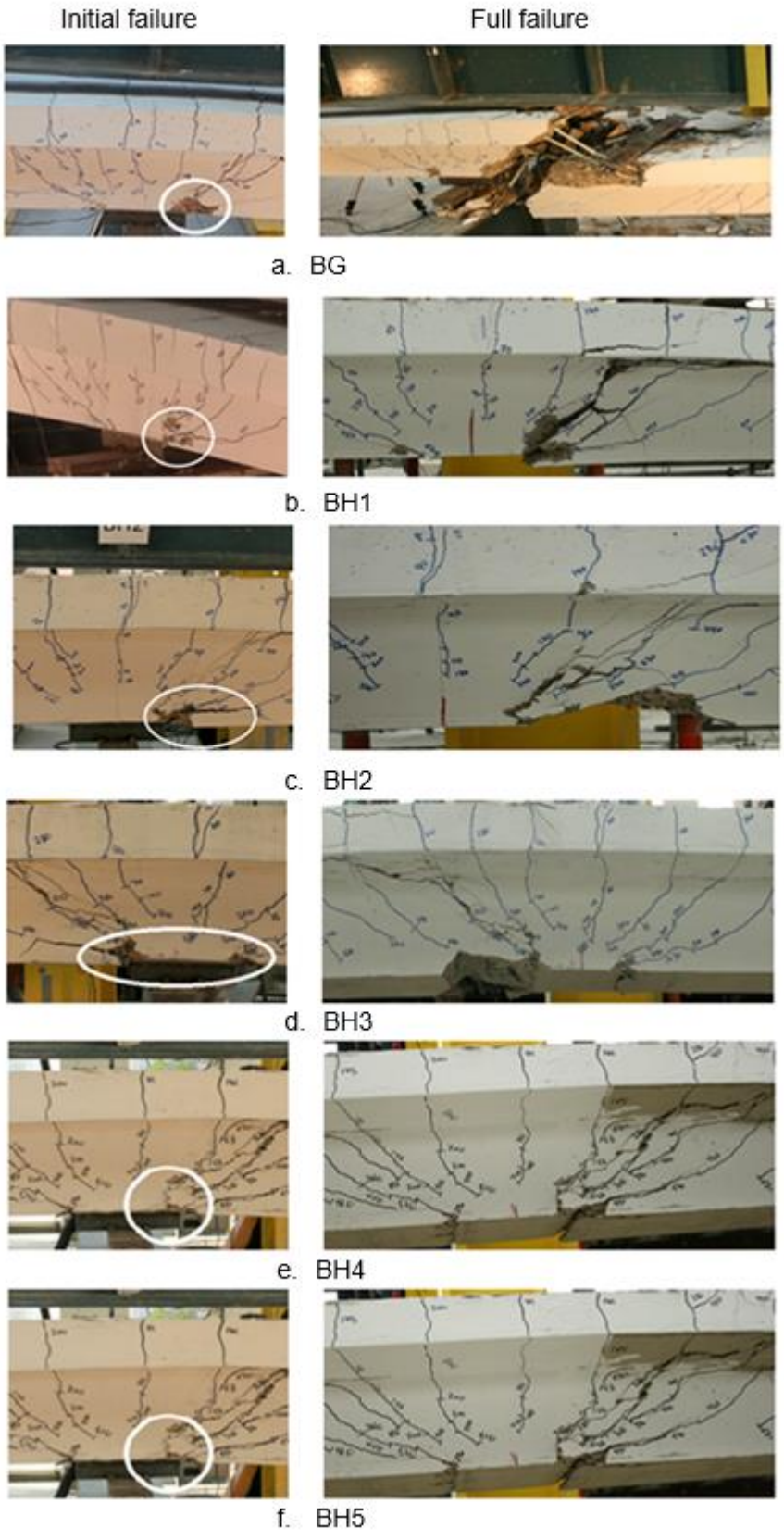

Figure 6: Modes of failure for the tested beams.

a. BG

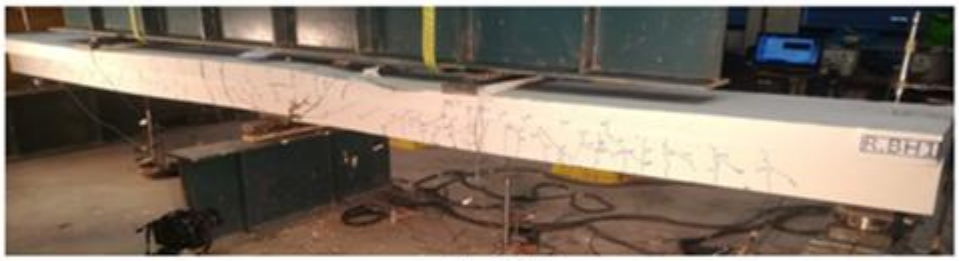

b. BH1

c. BH2

d. BH3

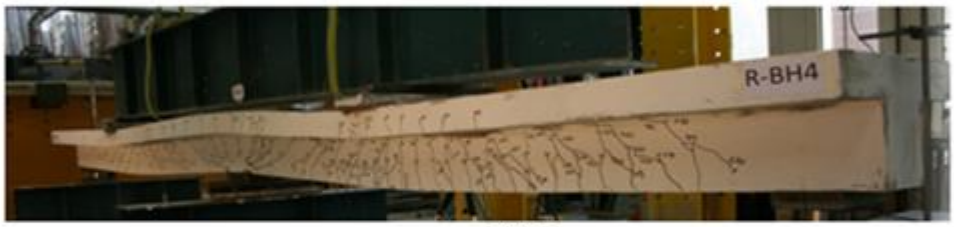

e. BH4

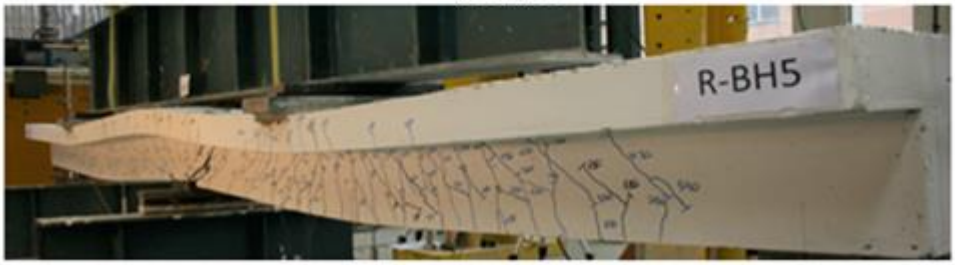

f. BH5

Fig. 7: The deformed shape of the tested beams (R stand for the right side).

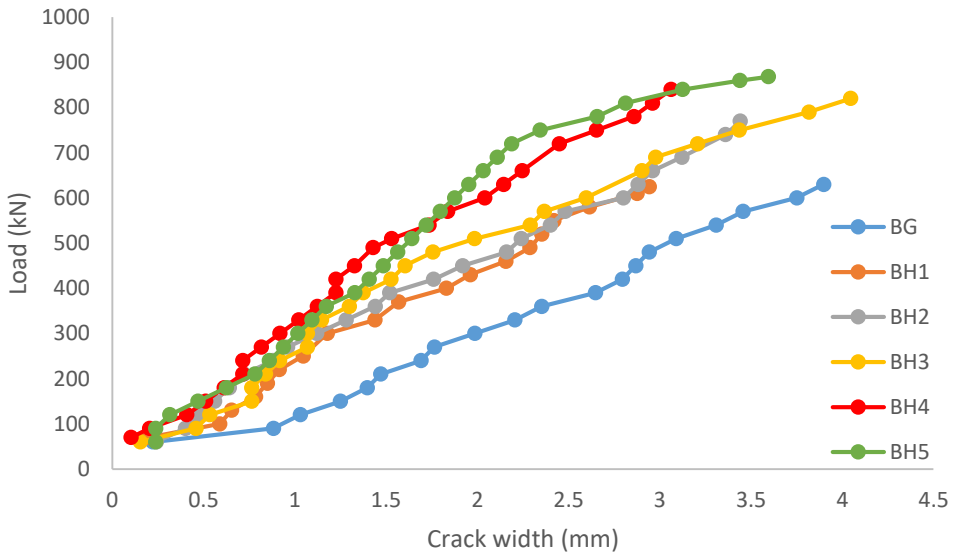

Figure 8: Crack width of tested beams at the middle-support section.

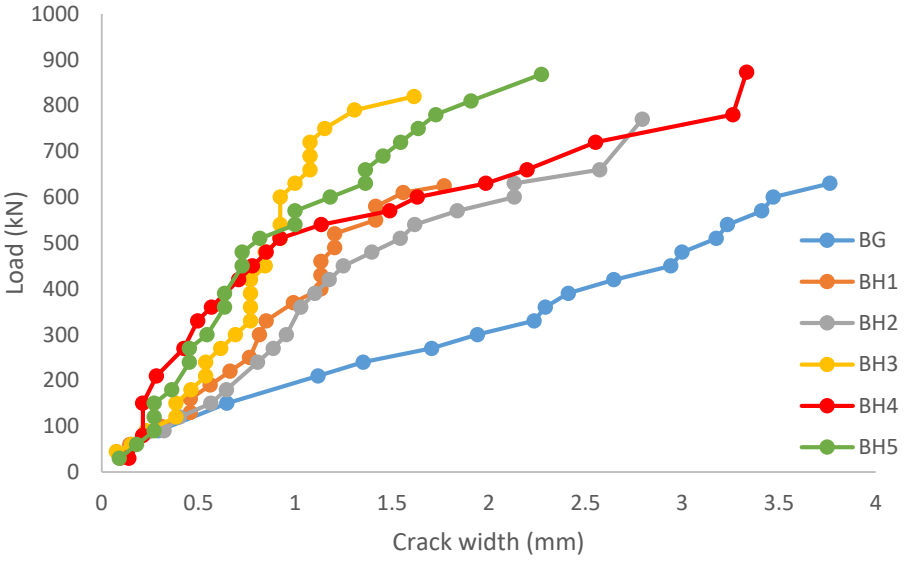

Figure 9: Crack width of tested beams at the mid-span section.

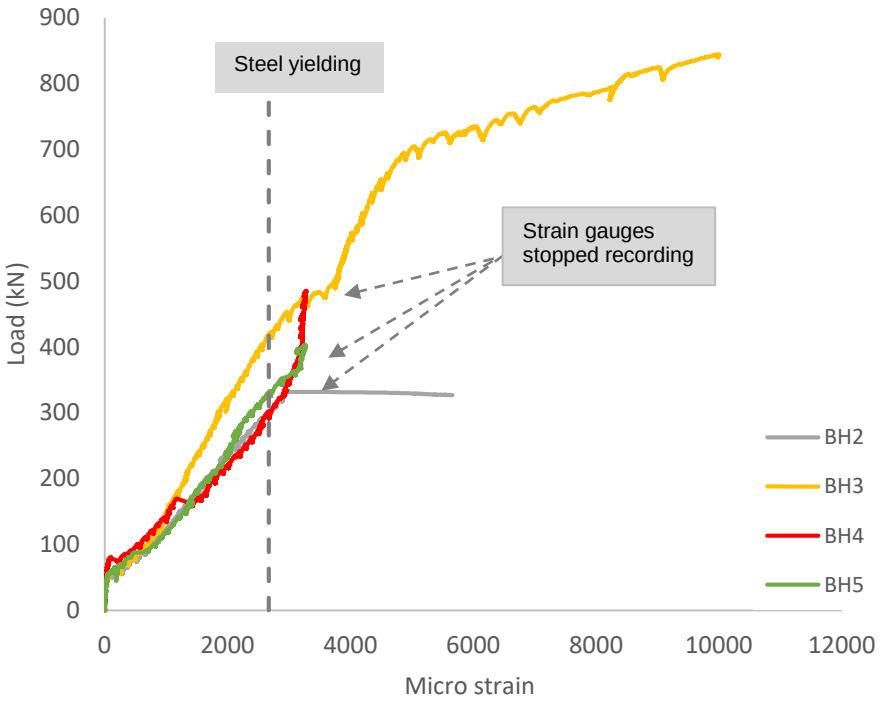

Figure 10: Variation of steel strain in the middle-support section.

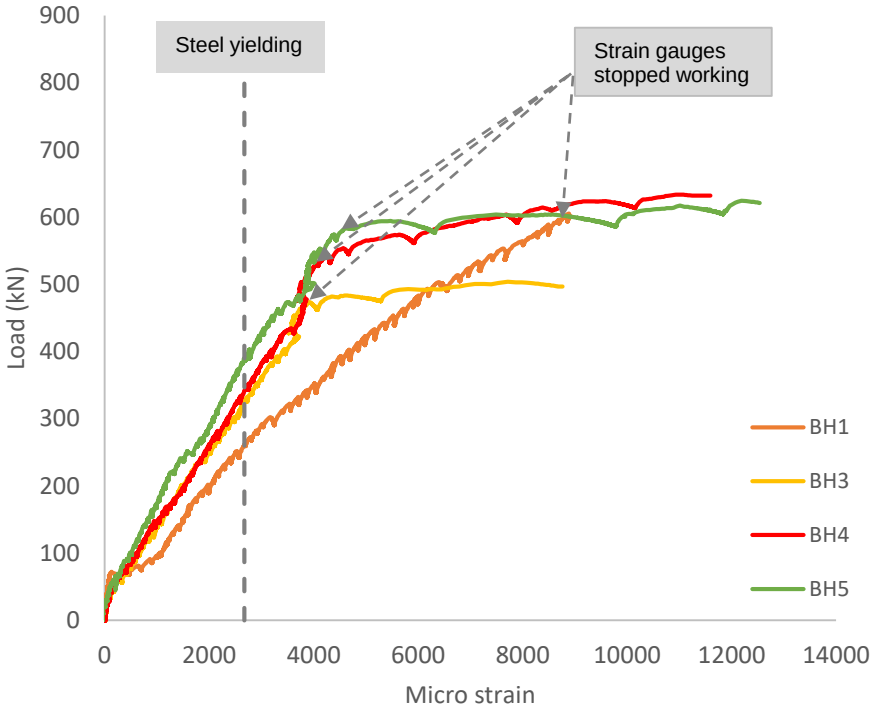

Figure 11: Variation of steel strain in the mid-span section.

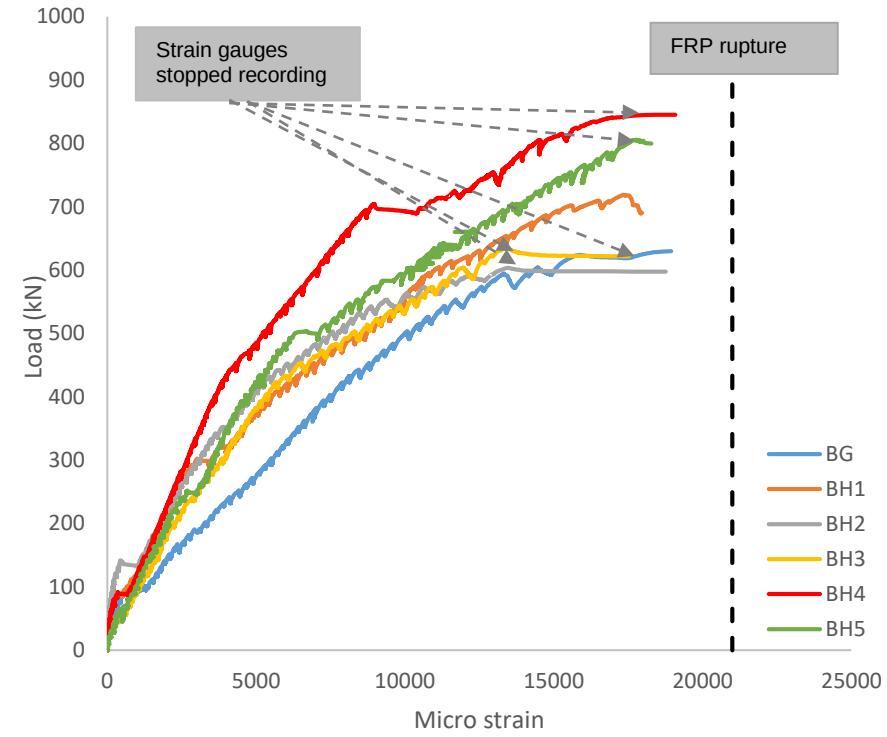

Figure 12: Variation of FRP strain in the mid-span section.

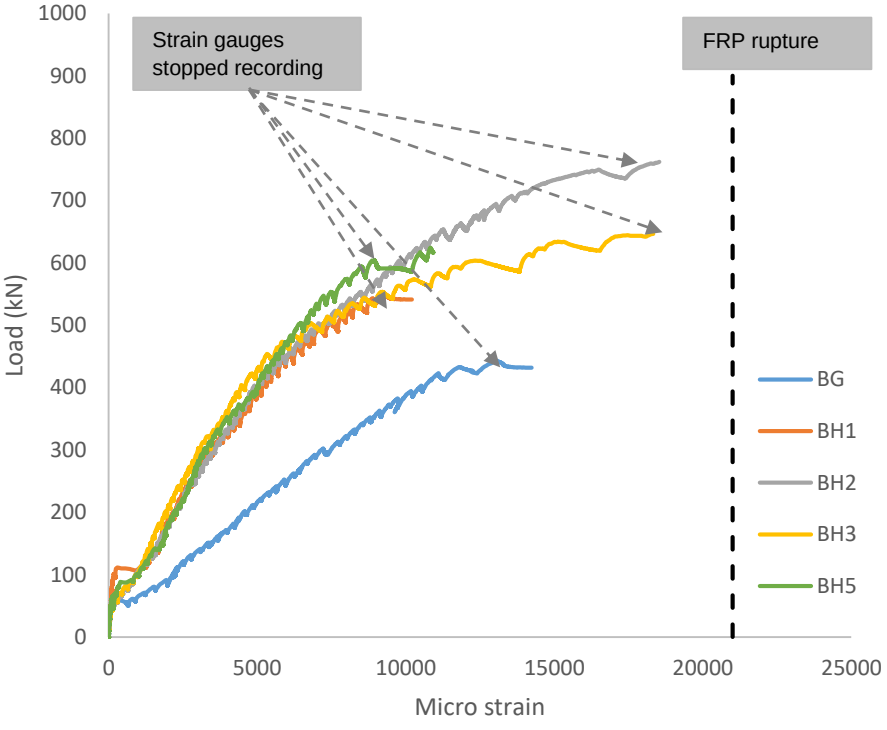

Figure 13:Variation of FRP strain in the middle-support section.

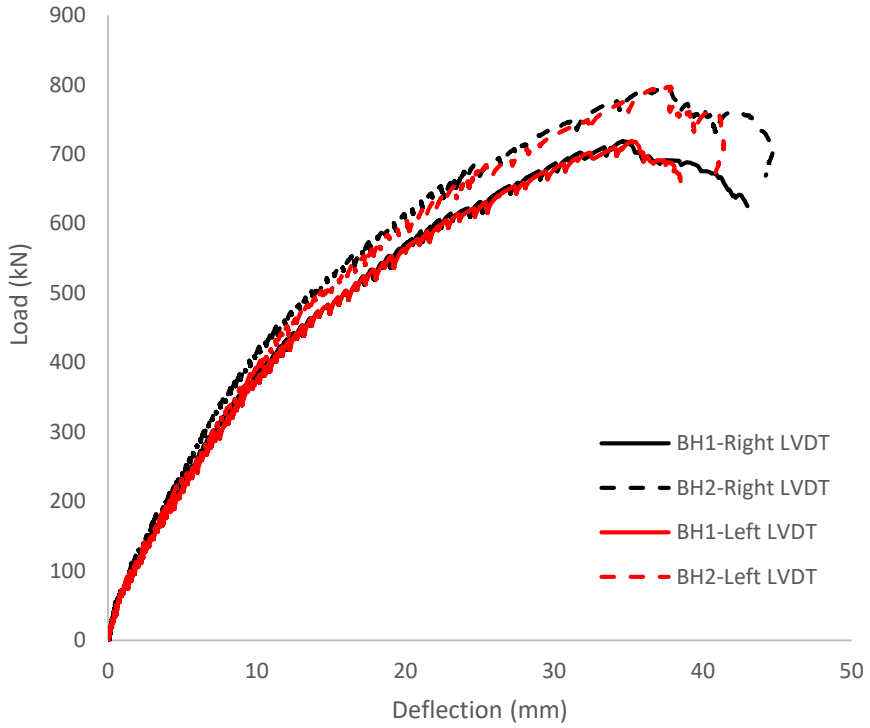

a. Comparison between the load-deflection measurements at both mid-span section for beams BH1 and BH2.

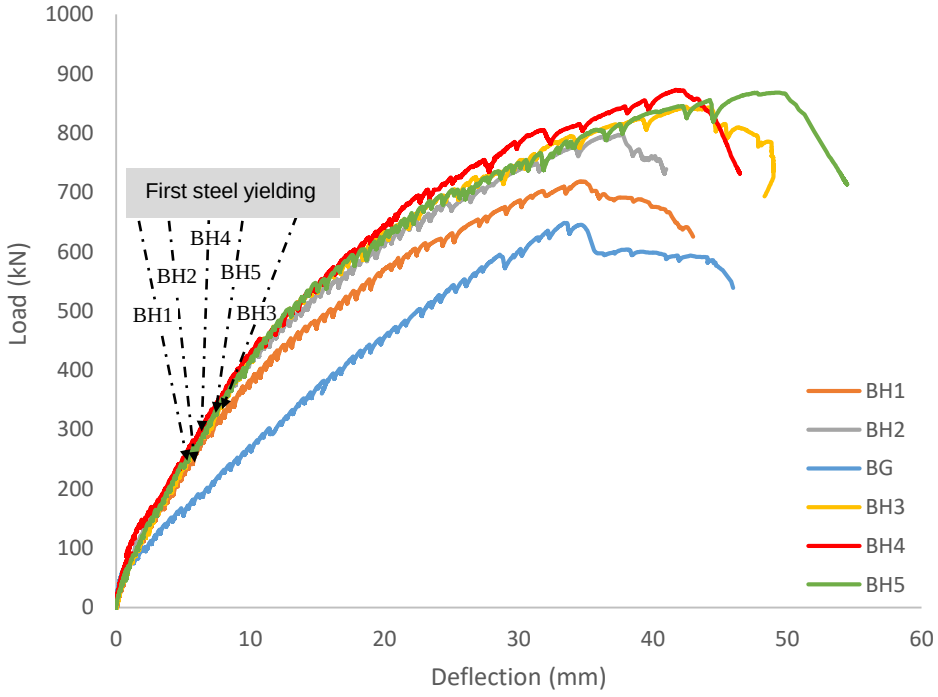

b. Load deflection beahviour at one mid-span section.

Figure 14: Load-deflection response of the tested beams.

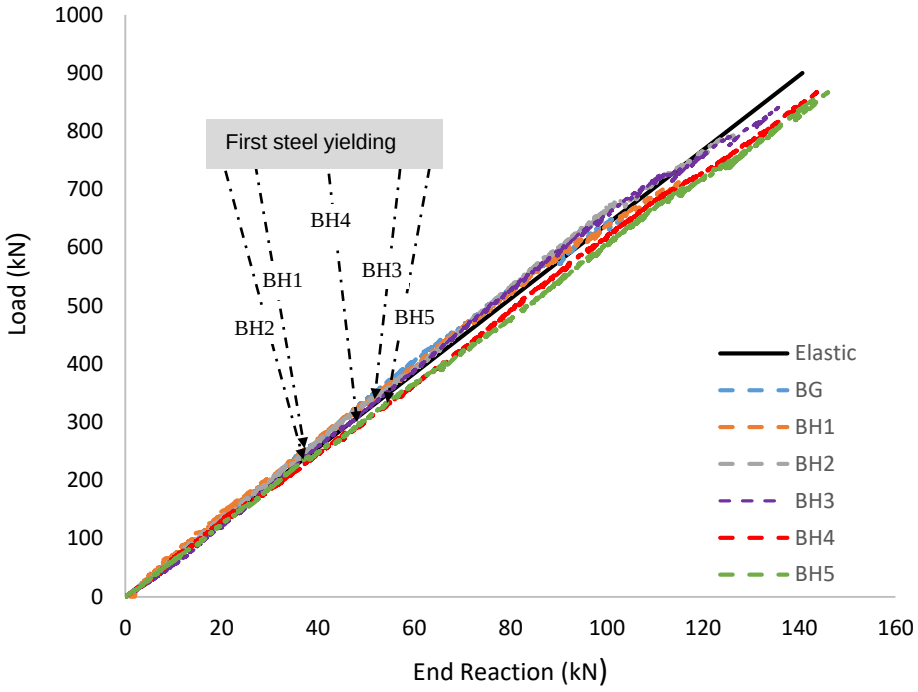

Figure 15: The measured end reactions against the total applied load of the tested beams.

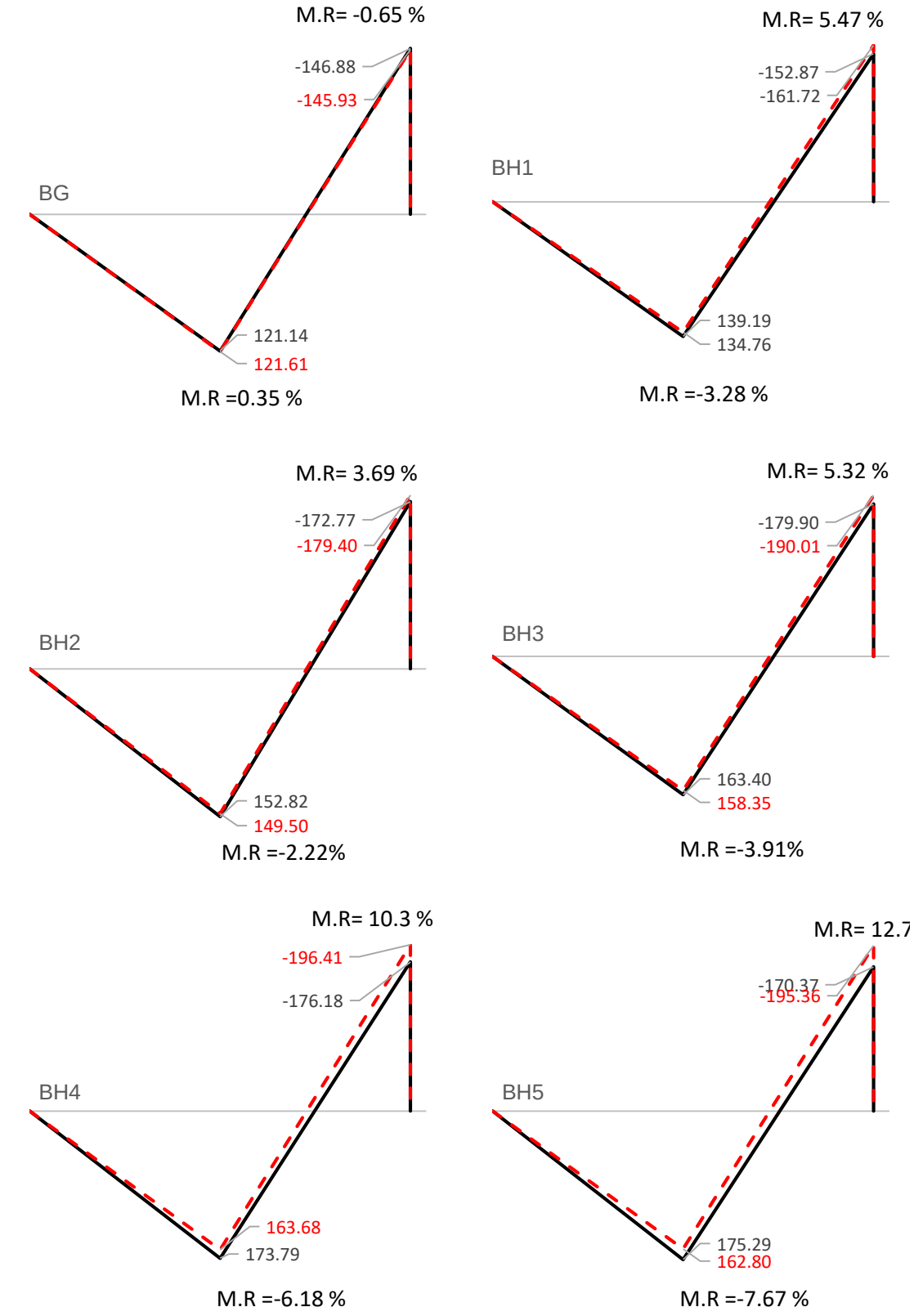

Figure 16: Moment redistribution for the tested beams.

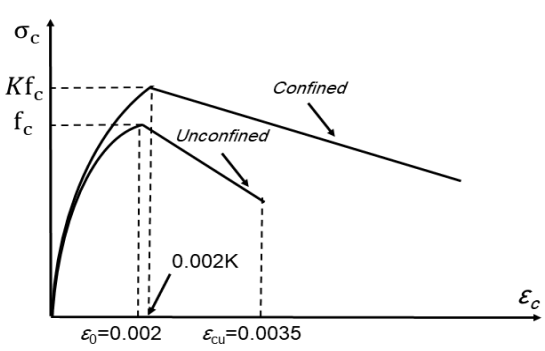

a. Concrete under compression

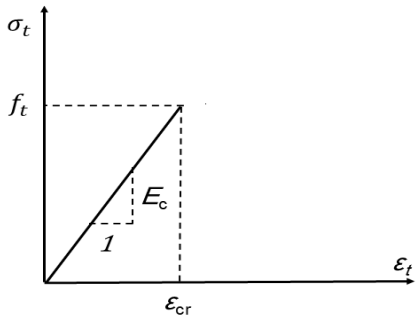

b. Concrete under Tension

Figure 17: Stress-strain relationship for concrete [26, 27].

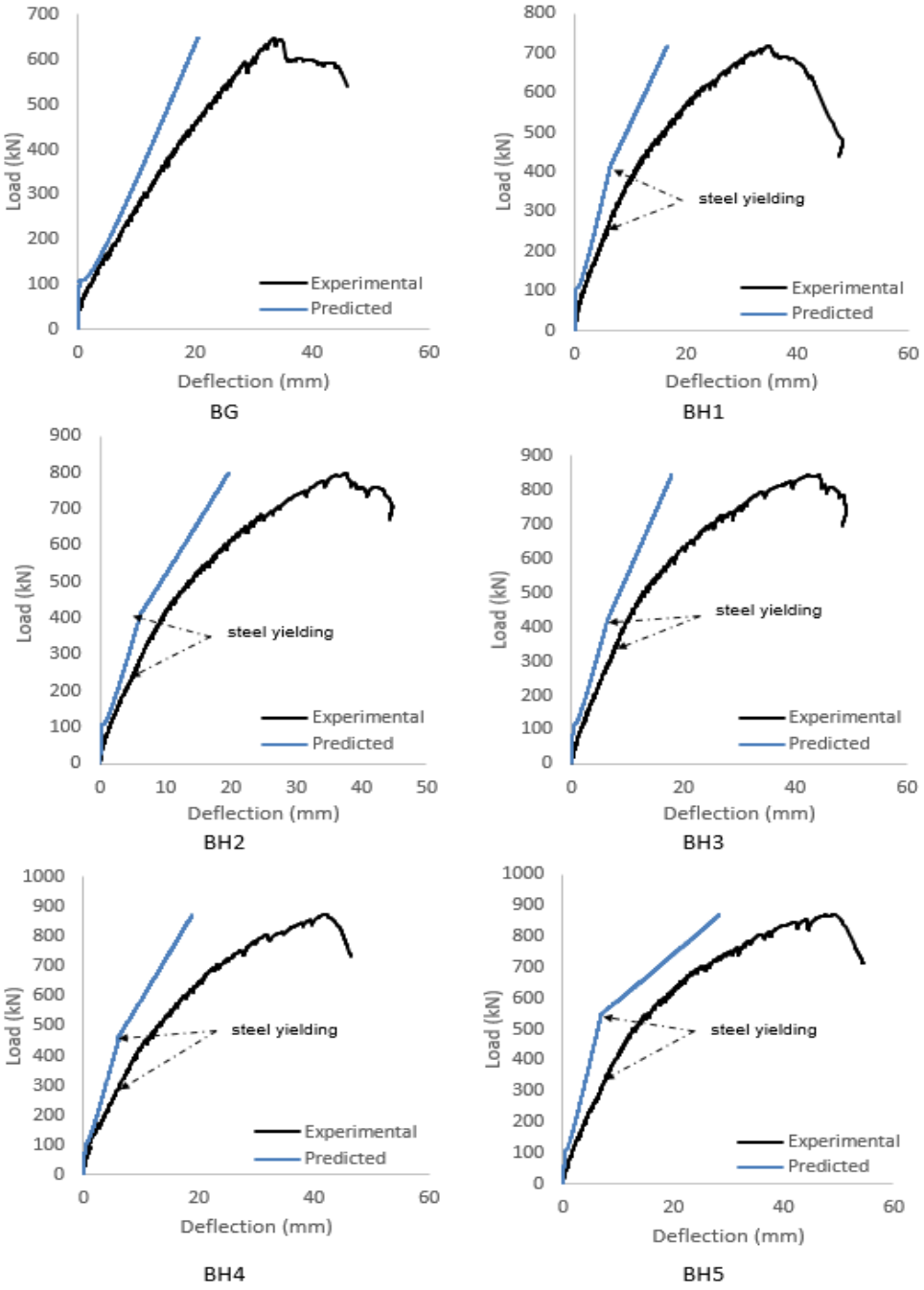

Figure 18: Prediction of load-deflection response.

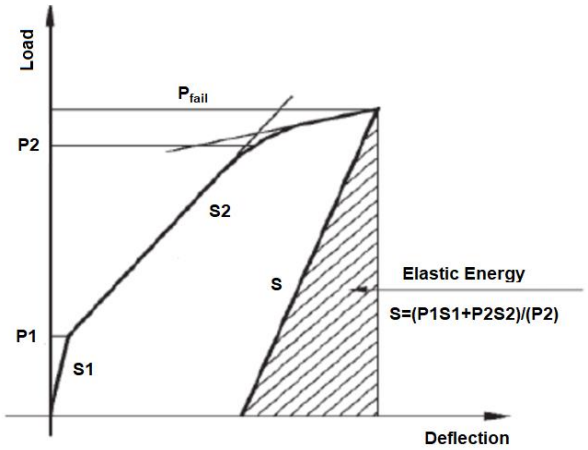

Figure 19:Total, elastic and inelastic energies [25].

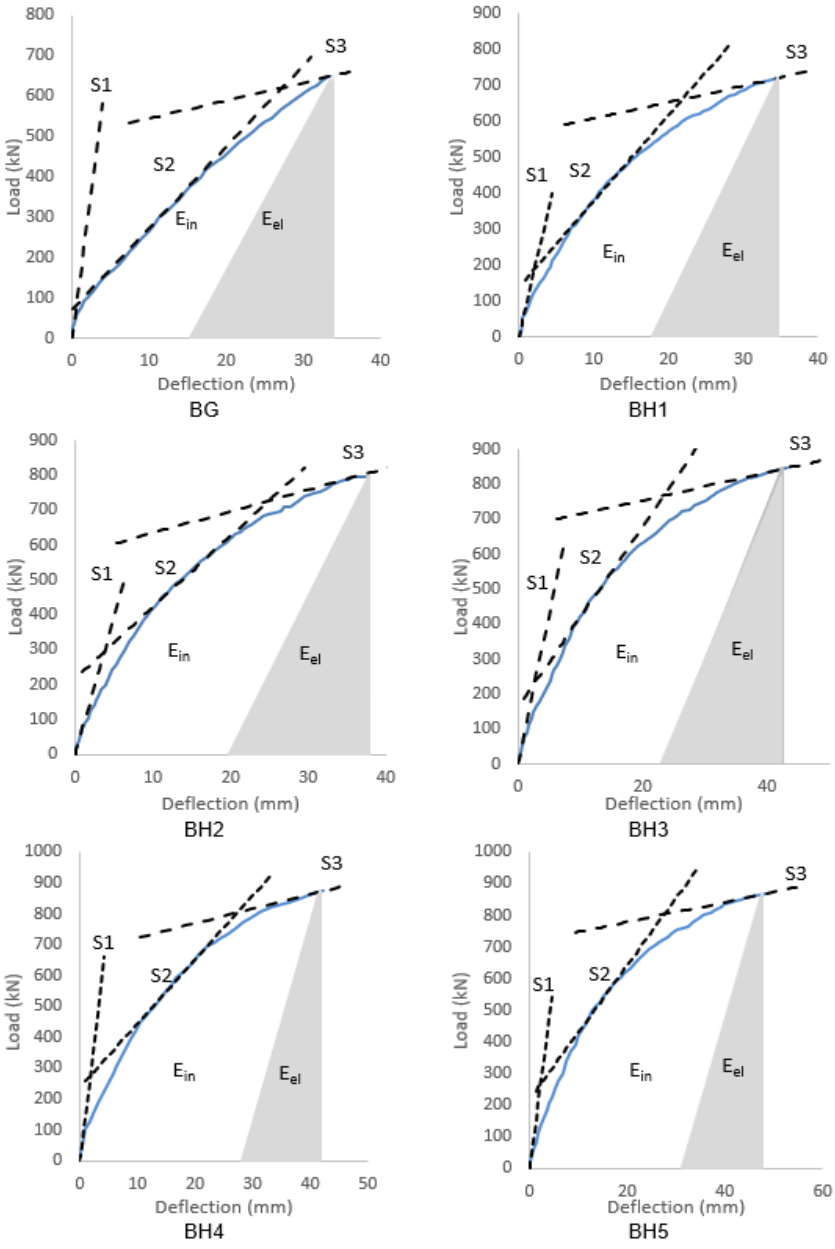

Figure 20: Total, elastic, and non-elastic energies for the tested beams using energy index.

List of tables

Table 1: Reinforcement details for the tested beams.

Specimens	Sagging				Hogging				Objective
	GFRP	ρ_f%	Steel	ρ_s%	GFRP	ρ_f%	Steel	ρ_s%	
BG	4Φ16	0.55	-	-	3Φ16	1.0	-	-	Control GFRP
BH1	3Φ16	0.41	2Φ16	0.31	2Φ16	0.69	2Φ10	0.30	Control Hybrid
BH2	3Φ16	0.41	2Φ16	0.31	3Φ16	1.0	2Φ10	0.3	Effect of increasing GFRP in hogging
BH3	3Φ16	0.41	2Φ16	0.31	2Φ16	0.69	2Φ16	0.77	Effect of increasing steel in hogging
BH4	4Φ16	0.55	2Φ16	0.31	2Φ16	0.69	2Φ10	0.30	Effect of increasing GFRP in sagging
BH5	3Φ16	0.41	3Φ16	0.46	2Φ16	0.69	2Φ10	0.30	Effect of increasing steel in hogging

$\rho_{sagging} = \frac{A_{s,f}}{b_f d}$, $\rho_{hogging} = \frac{A_{s,f}}{b_w d}$ where d is the depth of is the depth of FRP reinforcement (=262 mm)

Table 2: Mechanical properties of reinforcement bars.

Material	Diameter (mm)	* Area (mm^2)	**Area (mm^2)	Yielding strength (MPa)	Tensile strength (MPa)	Modulus of elasticity (GPa)
GFRP	16	180	184.4	-	923	48
GFRP	10	73	75.9	-	1101	62
steel	16	201	-	532	626	200
Steel	10	78.5	-	500	556	203

* Area provided by the manufacturer
** Equivalent area measured according to ACI440.3R-12

Table 3: Concrete properties for the tested beams.

beam	f_{cu} (MPa)	f_c`(MPa)	f_{ct} (MPa)
BG	57.8	49.1	2.94
BH1	57.4	48.8	3.04
BH2	58.2	49.5	3.34
BH3	61.6	52.4	2.48
BH4	55.8	47.4	2.39
BH5	57.3	48.7	2.42

f_{cu}: is the cube compressive strength f_c`: is the equivalent cylinder compressive strength assumed equal to 0.85fcu , f_{ct} is the concrete tensile compressive strength by cylinder splitting test.

Table 4: First cracking load, cracking width, steel yielding load and the total failure load of the tested beams.

Beam notation	First cracking load (kN)		Steel yielding load (kN)		Total load (kN)
	Mid-span	Middle-support	Mid-span	Middle-support	
BG	50	60	N.A	N.A	648.6
BH1	30	70	251.5	N.A	718.7
BH2	40	60	N.A	247.2	797.3
BH3	45	60	337.8	388.47	844.5
BH4	30	75	341.9	292.5	872.9
BH5	40	60	389.3	333.7	868.2

Table 5: Prediction of moment capacity of HRCT-beams using ACI 440.2R-17.

Beam notation	Sagging moment section			Hogging moment section				
	M_{ex}	M_{cl}	$\frac{M_{cl}}{M_{ex}}$	M_{ex}	M_{cl}	$\frac{M_{cl}}{M_{ex}}$	M_{cl} Confined concrete	$\frac{M_{cl}}{M_{ex}}$
BG	121.1	167.39	1.38	145.93	116.43	0.80	172.93	1.19
BH1	139.2	174.66	1.25	152.87	105.81	0.70	158.16	1.03
BH2	152.8	175.93	1.15	172.77	117.94	0.69	186.26	1.08
BH3	163.4	176.00	1.08	179.90	128.79	0.71	187.11	1.04
BH4	173.8	195.03	1.12	176.18	105.09	0.61	157.36	0.89
BH5	175.3	188.83	1.08	170.37	104.13	0.62	157.21	0.92
Average			1.18			0.69		1.03
Standard deviation			22.8%			34.9%		11.0%

Note: M_{ex}, M_{cl} are the experimental and calculated moment capacity respectively.

Table 6: The neutral axis depth, the cracked and the yielding moment of inertia for T-section beams.

The neutral axis depth as a function of c	
Mid-span (N.A in flang)	$c^2 + \left(\frac{2(n_f A_f + n_s A_s + n_{f2} A_{f2} + (n_{f1}-1)A_{f1})}{b_f}\right) c$ $- \frac{2(n_f A_f d_f + n_s A_s d_s + n_{f2} A_{f2} d_{f2} + (n_{f1}-1)A_{f1} d_{f1})}{b_f} = 0$
Middle-support (N.A in web)	$c^2 + \left(\frac{2((n_f-1)A_f + (n_s-1)A_s + n_{f2} A_{f2} + n_{f1} A_{f1} + n_{s1} A_{s1})}{b_w}\right) c$ $- \frac{2\left((n_f-1)A_f d_f + (n_s-1)A_s d_s + n_{f2} A_{f2} d_{f2} + n_{f1} A_{f1} d_{f1} + n_{s1} A_{s1} d_{s1}\right)}{b_w} = 0$
The cracked moment, I_{cr}	
Mid-span (N.A in flang)	$I_{cr} = \frac{b_f c^3}{3} + n_f A_f (d_f - c)^2 + n_s A_s (d_s - c)^2 + n_{f2} A_{f2} (d_{f2} - c)^2$ $+(n_{f1}-1)A_{f1} (d_{f1} - c)^2$
Middle-support (N.A in web)	$I_{cr} = \frac{b_f c^3}{3} + (n_f-1)A_f (d_f - c)^2 + (n_s-1)A_s (d_s - c)^2 + n_{f2} A_{f2} (d_{f2} - c)^2$ $n_{f1} A_{f1} (d_{f1} - c)^2 + n_{s1} A_{s1} (d_{s1} - c)^2$
The yielding moment, I_y	
Mid-span (N.A in flang)	$I_{cr} = \frac{b_f c^3}{3} + n_f A_f (d_f - c)^2 + n_{f2} A_{f2} (d_{f2} - c)^2 + (n_{f1}-1)A_{f1} (d_{f1} - c)^2$
Middle-support (N.A in web)	$I_{cr} = \frac{b_f c^3}{3} + (n_f-1)A_f (d_f - c)^2 + n_{f2} A_{f2} (d_{f2} - c)^2 n_{f1} A_{f1} (d_{f1} - c)^2$ $+n_{s1} A_{s1} (d_{s1} - c)^2$

Note: c is the neutral axis depth, b_f is the flange width, and b_w is the web depth, n_f, n_s, n_{s1} , n_{f1} , n_{f2} are the elastic modulus ratio between bottom FRP, bottom steel, top steel, top FRP, bottom flange FRP reinforcement and concrete, respectively. , d_f, d_s, d_{f1}, d_{f2} are depths of bottom FRP, bottom steel, bottom, top FRP, bottom flange FRP reinforcement, respectively is the neutral axis depth; A_f, A_s, A_{s1}, A_{f1}, A_{f2} are the area of bottom FRP, bottom steel, top steel, top FRP, bottom flange FRP reinforcement, respectively

Table 7: The energy ductility index for the test beams.

Beam	Energy method				
	E total (kN.mm)	S	E elastic	μc	$\frac{\mu e - \mu e_{BG}}{\mu e_{BG}} \times 100\%$
BG	12917.1	35.7	5900.3	1.59	-
BH1	16726.9	42.9	6014.6	1.89	18.2
BH2	20145.7	44.3	7167.0	1.91	19.1
BH3	25287.6	44.9	7943.7	2.09	30.7
BH4	25399.9	65.8	5790.0	2.69	68.3
BH5	29839.3	53.0	7110.2	2.73	70.5

S is the weighted average slop of the two initial straight lines of the load-deflection curves as shown in Fig.19